aerospace

MDPI

Article

Ice Cavitation Deicing for Aerospace Applications

Victor F. Petrenko

Thayer School of Engineering, Dartmouth College, Hanover, NH 03755, USA; victor.f.petrenko@dartmouth.edu

Abstract

Ice accretion along aircraft leading edges, particularly at stagnation line parting strips, remains difficult to remove using conventional electrothermal anti-icing systems. These systems require continuous high-power heating to maintain the stagnation region above the melting point, often exceeding 10–12 kW/m^2. This study introduces an Ice Cavitation Deicer (ICD) that removes ice through rapid, localized cavitation generated within a thin melt layer formed at the ice–surface interface. In the proposed approach, a short pulse of electric current melts a 1–10 μm interfacial layer and causes a cavitation impulse of approximately 1–10 MPa. This impulse ejects the stagnation-line ice in a direction normal to the surface, often against the external airflow, enabling the immediate aerodynamic removal of the remaining ice. Analytical modeling based on the energy conservation principle was used to determine the optimal foil geometry, thermal pulse parameters, thermal stress, and material selection. Experiments with various metallic foils and substrate materials validated the predicted ejection behavior. The impulses were sufficient to fracture and eject ice 1–10 mm thick. The observed ice fragment velocities varied from 1 m/s to 10 m/s. Compared with conventional thermal anti-icing, the ICD concept reduces power consumption by approximately two orders of magnitude while offering rapid and reliable leading-edge deicing. The low power requirements, rapid response, and compatibility with thin-foil heater architectures make ICD a promising technology for both conventional and electrified aircrafts, UAVs, rotorcrafts, and other platforms where power availability is limited. This manuscript presents the first theoretical and experimental research on the ICD method and is a concept-proof work. Further research and development are required before the ICD is ready to be tested in flight.

Keywords: ice cavitation deicer (ICD); pulse electrothermal deicer (PETD); cavitation pressure; stagnation-line deicing; leading-edge deicing; COMSOL Multiphysics 5.4

Check for updates

Academic Editor: Konstantinos Kontis

Received: 12 January 2026
Revised: 6 February 2026
Accepted: 21 February 2026
Published: 27 February 2026

Copyright: © 2026 by the author. Licensee MDPI, Basel, Switzerland. This article is an open access article distributed under the terms and conditions of the Creative Commons Attribution (CC BY) license.

1. Introduction

Ice accretion on aircraft wings and engine inlets is a persistent hazard in aviation. When supercooled water droplets impact an airfoil, they may freeze on contact and form ice layers that alter the aerodynamic shape, reduce lift, increase drag, and in severe cases, lead to flow separation and loss of flight stability. The region of the wing leading edge that is most difficult to protect is the stagnation-line parting strip, where the local airflow velocity approaches zero and convective momentum transfer is minimal. Ice in this region adheres strongly to the surface and is resistant to both aerodynamic removal and mechanical shedding.

Conventional electrothermal anti-icing systems address this problem by supplying continuous high-power heating to the stagnation region to maintain it above the ice melting point. Typical power densities may reach 10–12 kW/m^2. The high power density imposes

a substantial energy burden on aircraft electrical systems and limits their applicability to smaller platforms, such as unmanned aerial vehicles. Alternative pulse-based electrothermal deicers (PETDs [1]) reduce power by melting a thin interfacial layer between ice and the substrate. Since the PETD patent application date (February 2000), the method has been used in numerous applications. Petrenko et al. [2] systematically presented the PETD concept, theory, computer simulations, extensive laboratory test data, and large-scale implementations across multiple applications (aircraft, bridges, windshields, roofs, and ice makers). This paper demonstrated energy savings of up to ~99% over conventional thermal de-icing and it remains the core reference for PETD research. The recent publication by Khodakarami et al. [3] presented a very detailed and thorough study of electrothermal pulse deicing capable of efficient and rapid removal of ice from aircraft wings. This publication also provides a comprehensive review of PETD research and development. However, because stagnation-line ice is not readily lifted by aerodynamic forces, PETDs alone are insufficient to remove ice from the critical region of the airfoil. The addition of an Ice Cavitation Deicer (ICD) to the PETD can solve the problem of cleaning the leading edges of airfoils without incurring a high energy cost. In an ICD, a thin metallic foil is pulse-heated above the water cavitation temperature (≈300 °C). That generates a rapid pressure impulse within the interfacial melt layer. This impulse can reach approximately 10–20 MPa [4,5], which is sufficiently high to fracture and eject ice in the direction normal to the surface, even against the external airflow.

The idea of leveraging high water vapor pressure to improve PETD performance was first proposed in 2010 by Petrenko [6], but it has never been investigated. When combined with an upstream PETD pulse that forms a thin melt layer (typically 0.01–0.1 mm thick), the ICD enables the rapid removal of stagnation-line ice that would otherwise remain attached.

In this study, the underlying theory of ICD operation was developed based on the energy conservation principle, thermal and mechanical constraints were evaluated, and COMSOL Multiphysics 5.4 FEA simulations were used to optimize the foil geometry, heating rates, and material selection. Experimental demonstrations with metals and laminate foils confirmed the predicted cavitation-induced ice ejection. The results show that the ICD concept can reduce the stagnation line deicing power up two orders of magnitude relative to conventional continuous electrothermal systems, offering a compact, energy-efficient, and fast-acting solution for aerospace deicing. The new deicing method can complement existing cyclic and PETD electrothermal deicing technologies over the entire spectrum of atmospheric conditions and aircraft types where cycling electrothermal deicing technologies are in current use.

2. ICD Concept and Preliminary Criteria for the Selection of ICD Materials

Predicting cavitation is a formidable task, particularly in water [7]. Despite significant efforts and achievements, the study is still ongoing. However, no theoretical studies on ice cavitation have been performed to date. Because of the lack of information about ice cavitation, it is not productive to begin experimenting with a new phenomenon without an approximate set of calculations and numerical estimates of its effects on the system.

The following analytical and computer simulation analyses did not pretend to be accurate ICD theories; however, they have proven to be useful for selecting candidate materials and determining a range of appropriate experimental conditions.

First, numerical calculations based on the energy conservation law (ECL) were performed. Although the ECL is an approximation, it is an effective tool. This study assumes that the electric energy initially stored in an ICD capacitor is used to heat a thin

metal foil, heat-diffusion layers of the substrate and ice, and the resistive components of power electronics.

Figure 1 shows the ICD geometry used in this study. The metal foil was attached to the substrate (Warm PETD foil) using a high-temperature adhesive.

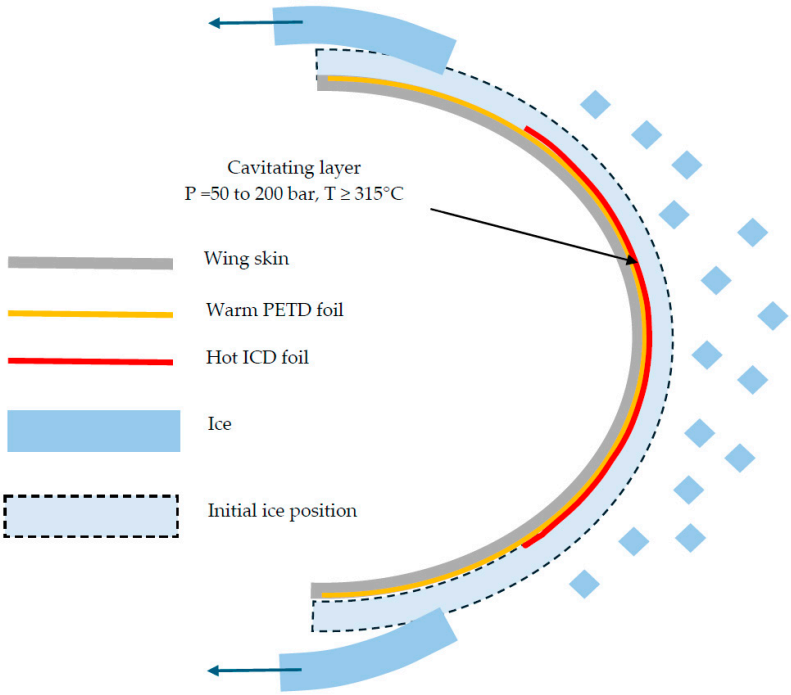


Figure 1. ICD geometry prior to expansion of the cavitation layer (yellow) of the melted ice. Combined PETD/ICD deicing system is shown.

2.1. Notations

Because the 45 variables are used in the theoretical part of the manuscript, for the reader's convenience, all the variables are listed in one place below.

B	magnetic flux density, T (tesla).
B_r	remanent magnetic flux density of a permanent magnet, T (tesla).
C_C	capacitance of an energy-storage capacitor, F.
E	elastic modulus, Pa.
g	acceleration due to gravity, m/s^2.
l	length, m.
L_{tot}	total inductance of the capacitor-discharge circuit, H.
M_{sat}	Saturation magnetization, A/m.
P_{cav}	water cavitation pressure.
$Psat$	saturation pressure of water vapor.
q_i	latent heat of ice melting, which is 333 kJ/kg.
q_w	latent heat of water evaporation.
Q_C	initial energy stored in the capacitor, J.
Q_{ICD}	density of the energy required for ICD (J/m^2).
Q_{tot}	total density of the energy requirement of an ICD, which includes the circuit losses (J/m^2).
r	aspect ratio, l/w.
R_{tot}	total serial resistance of the entire power circuit. This includes the resistance (ESR) of the capacitor, switch, metal foil, and lids, Ω.

$R_m = \rho_e \cdot r/t_m$	resistance of the metal foil, where t_m is the material thickness, Ω.
$R_{rest} = R_{tot} - R_m$	resistance of all other circuit components, lids, bus bars, ESR of the switch, and capacitor, Ω.
t_p	thermal pulse length, s.
T_0	initial temperature of the ICD, °C.
T_m	ice-melting temperature, 0 °C.
T_{ICD}	maximum (cavitation) temperature of the metal foil before cavitation occurs. $T_{ICD} = T_{evap}$ shown in some figures.
T_{no_ice}	maximum ICD temperature in the absence of ice, °C.
v_{ice}	maximum ice velocity, m/s.
V_0	initial capacitor voltage, V.
w	width, m.
z	normal to the ICD plane coordinate, m.
α	coefficient of thermal expansion (CTE), K^{-1}.
γ	C_P/C_V ratio of water vapor.

$$\lambda = \left(\frac{t_p \cdot k}{C \cdot \rho}\right)^{1/2} \text{ heat diffusion length, m.} \quad (1)$$

μ	shear modulus, Pa.
μ_0	permeability of vacuum, $4\pi \cdot 10^{-7}$, H/m.

$$\xi = \frac{R_{tot}}{2}\sqrt{\frac{C_C}{L_{tot}}} \text{ RCL-circuit damping factor.} \quad (2)$$

ρ	density, kg/m^3.
ρ_e	electrical resistivity, Ω·m.
ρ_v	water vapor density at atmospheric pressure, Pa.
ρ_{cav}	water vapor density at cavitation pressure, Pa.
σ	stress, Pa.
σ_{TS}	thermal stress, Pa.
σ_{yield}	yield stress, Pa.
ΔT	maximum temperature difference between two points in a material.

The subscripts s, m, i, and w denote the substrate, metal, ice, and water, respectively.

2.2. Calculations of the ICD Energy Requirement

The approximate energy requirement for heating ICD foil from T_0 to T_{ICD} can be determined by applying the Energy Conservation Law (First Law of Thermodynamics) as follows:

$$Q_{ICD} = (T_{ICD} - T_0)\cdot(\rho_S \cdot C_S \cdot \lambda_S + t_m \cdot \rho_m \cdot C_m) + q_i \cdot \rho_i \cdot \lambda_w + (T_m - T_0)\cdot C_i \rho_i \cdot \lambda_i + (T_{ICD} - T_m)\cdot C_w \cdot \rho_w \cdot \lambda_w \quad (3)$$

where all the variables were clearly defined in the Notations. Equation (3) assumes that the energy delivered to the ICD is distributed through heat conduction across the metal foil, heat diffusion layers of the substrate, ice, and melted layer (i.e., water). It also includes the latent heat of ice melting within the heat diffusion length of water. The choice of λ_w instead of λi creates the main uncertainty in this simplified approach. But because the main contributor to Q_{ICD} is $(T_{ICD} - T_0)\cdot(t_m \cdot \rho_m \cdot C_m)$ term, the wrong choice of λ is less important. Notice that the heat diffusion length in ice, λ_i, is several times greater than that of water, λ_w. Equation (3) provides a simple way to calculate the initial parameters for ICD

design and optimization. More accurate than Equation (3) results were obtained through one-dimensional COMSOL Multiphysics 5.4 Heat Transfer simulation in Section 2.9.

Not all the energy stored in the capacitor is used to heat the metal foil and interfacial layers of the materials. A portion of the stored energy is lost in the components of an electric circuit. Therefore, the total ICD energy requirement, Q_{tot}, exceeds Q_{ICD}:

$$Q_{tot} = \frac{Q_{ICD} \cdot R_{tot}}{R_m} \tag{4}$$

As shown in Figure 2, Q_{tot} initially decreased with an increase in the aspect ratio of the foil, r, and then increased with a further increase in r. The initial decrease in Q_{tot} was caused by an increase in the resistance of the foil and lower losses in the rest of the electric circuit. The subsequent increase in Q_{tot} is due to the increase in the circuit time constant t_p, which results in greater heat diffusion into ice and substrate.

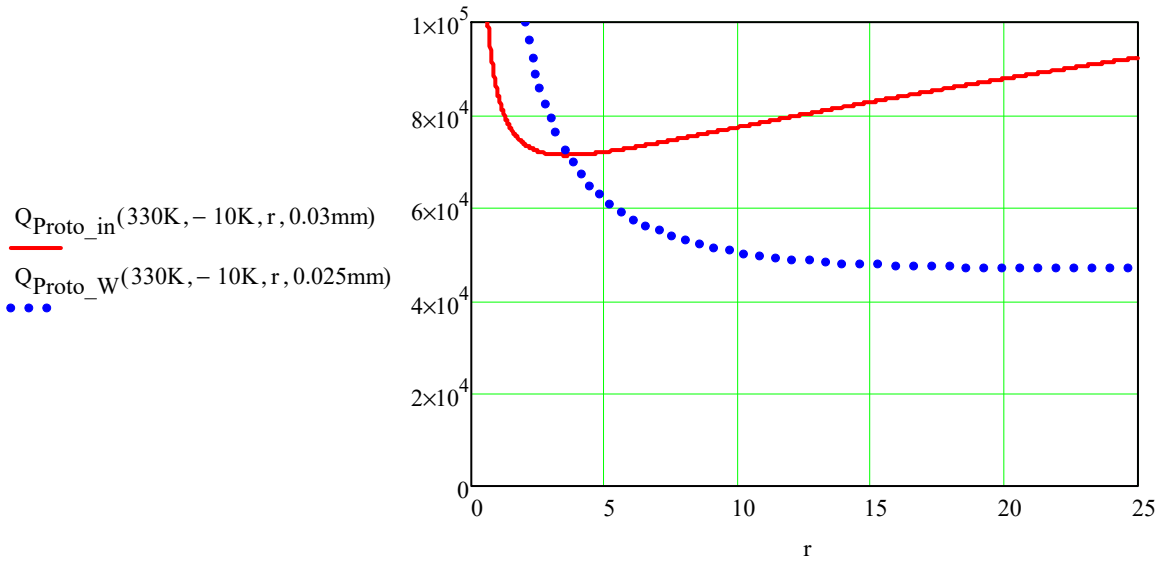


Figure 2. Total ICD energy requirement, Q_{tot} (J/m^2) vs. aspect ratio of a foil r, calculated with Equations (3) and (4) for the 0.03 mm Invar foil (solid red line) and for the Tungsten 0.025 mm foil (blue dotted line). The base material was porcelain ceramic. The sub "Proto" was used by MathCAD 15.

The maximum temperature of the foils was T_{ICD} = 330 °C and T_0 = −10 °C. The heat diffusion length was calculated using Equation (1), where $t_p = R_{tot} \cdot C_C$ was the time constant of an over-damped RCL circuit. The sub "Proto" instead of "ICD" was used in our MathCad calculations.

The minimum ICD energy requirement shown in Figure 2 is common for all foil materials that were simulated and analyzed. The foil material properties are presented in Table A1 in Appendix A. The properties of the substrates are listed in Table A2.

In Equation (1), t_p represents the "thermal pulse length," which is the time required for approximately 90% of the total energy stored in the capacitor to be delivered to the ICD. Computer simulations show that when the circuit is over-damped, $\xi >> 1$, t_p is approximately equal to $R_{tot} \cdot C_C$. The minimum duration of RCL (Resistor–Capacitor–Inductor) circuit discharge occurred when $\xi = 1$. In this case:

$$R_{tot_damped} = 2\sqrt{\frac{L_{tot}}{C_C}} \tag{5}$$

is the fully damped circuit resistance, ξ

$$t_{damp} = \frac{\sqrt{L_{tot}C_C}}{2} \quad (6)$$

is the electrical time constant of a fully damped circuit.

According to our computer simulation results (Section 2.6), the maximum ICD temperature of a fully damped RCL circuit was observed at the time:

$$t_{p_damp} \approx 2t_{damp} \quad (7)$$

For over-damped circuits, $\xi >> 1$:

$$t_p \approx R_{tot} \cdot C_C \quad (8)$$

In the following Section 2.5, "Cavitation Pressure of Water and Its Work," it is shown that the total mechanical momentum exerted on the ice due to the vapor pressure increases with an increase in t_p. Thus, circuits with a high dissipation factor ($\zeta >> 1$) have been employed in applications where significant mechanical momentum is required for ice removal, despite the higher energy demand associated with such designs. The main contributor to the ICD energy requirement is the $t_m \cdot \rho_m \cdot C_m$ product of Equation (3).

2.3. Overheating Ice-Free Areas of ICD

A critical parameter limiting ICD design is the maximum temperature T_{no_ice}, which is reached in the ice-free areas of the ICD. If the ICD is not properly designed, this temperature can easily exceed the maximum service temperature of the foil or substrate material. Using ECL, the following equation was derived for T_{no_ice} in the ICD's ice-free areas:

$$T_{no_ice} = \frac{Q_{ICD}}{\rho_m \cdot C_m \cdot t_m + \rho_S \cdot C_S \cdot \lambda_S} + T_0 \quad (9)$$

Given T_{ICD} and $T_{no_ice,}$ the ICD energy requirement in Equation (3) was minimized for all materials used in this study. The results of this optimization are presented in Table 1. The minimum ICD total energy requirement, Q_{tot}, was calculated for T_{evap} = 330 °C, T_{no_ice} = 400 °C, C_C = 1. 5,mF and R_{rest} = 14 mohm. The other properties of the materials are listed in Tables A1 and A2 in the Appendix A.

Table 1. The minimum ICD total energy requirement.

Material	$r = l/w$	Thickness mm	τ_p, ms	Q_{tot}, kJ/m^2
17-7PH SS	0.789	0.0194	0.061	42.9
Nb	4.8	0.035	0.072	48.25
W	11.6	0.031	0.072	49.1
Ti	1.466	0.034	0.072	49.3
Invar	0.69	0.019	0.071	49.1
SS440C	1.13	0.023	0.072	49.4
SS304	0.922	0.023	0.072	49.3

Surprisingly, the minimal Q_{tot} was almost the same for all materials because Q_{tot} depends mainly on T_{evap} and T_{no_ice}, as illustrated in Figures 3 and 4.

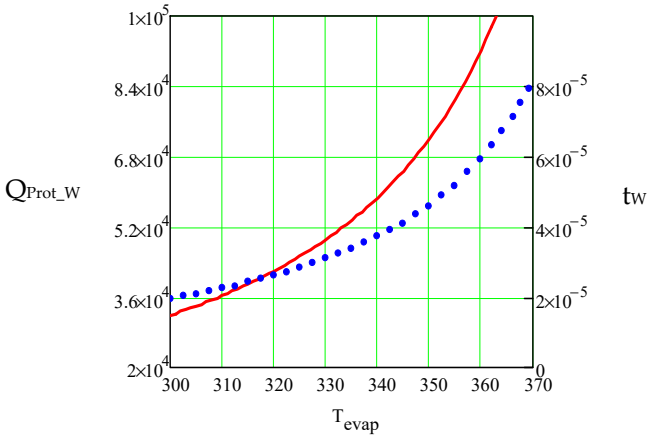


Figure 3. The optimized total energy density requirement, Q_{Prot_W}, J/m^2 (red solid line), and the optimized tungsten ICD foil thickness, t_W, m, (blue dotted line) vs. temperature of the ice-free areas. T_{evap} = 330 °C, C_C = 1.5 mF, and R_{rest} = 14 mohm. The sub "Prot_W" instead of "tot" was used in our MathCad calculations. W in the subscript is the chemical symbol for tungsten. MathCad 15.

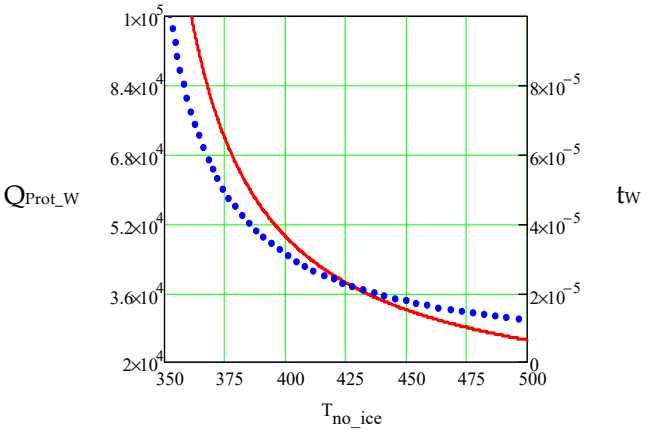


Figure 4. Total energy density requirement, Q_{Prot_W}, J/m^2 (red solid line), and tungsten ICD foil thickness, t_W, m, (blue dotted line) vs. maximum ICD temperature, $T_{evap} = T_{ICD}$. T_{no_ice} = 400 °C, C_C = 1.5 mF, and R_{rest} = 14 mohm. The sub "Prot_W" instead of "tot" was used in our MathCad calculations. W in the subscript is the chemical symbol for tungsten. MathCad 15.

2.4. Thermal Stress of ICD

Another design challenge for ICD is the high thermal stress of the metal foil and substrate material. When a material is constrained, the maximum thermal stress can be estimated as

$$\sigma_{TS} = \Delta T \cdot \alpha \cdot E \quad (10)$$

For a material to withstand multiple ICD pulses, its yield or/and compression strength should be higher than the maximum thermal stress:

$$\sigma_{yield} > \sigma_{TS} \quad (11)$$

Tables A1 and A2 of Appendix A present a comparison of σ_{yield} and σ_{TS} of the materials used in this study for $\Delta T = 400$ K. As can be seen, not all the materials tested or analyzed satisfied the requirements of Equation (11). The most probable location of the maximum thermal stress in the metal foils was the interfaces with the cold electrical busbars. This stress can be effectively reduced by heating the busbars using the same ICD electric pulse. The highest temperature gradients in the substrates occurred at the interface with hot metal foils.

This section addresses the classical thermo-mechanical shear-lag problem of a thin, stiff metallic foil bonded to a rigid substrate by a compliant adhesive layer and subjected to thermal loads. The problem is characterized by large in-plane aspect ratios and a strong stiffness contrast between the foil and adhesive, conditions under which full three-dimensional finite element modeling becomes computationally inefficient and numerically ill-conditioned.

The analytical framework employed in this study is rooted in the classical shear-lag theory originally introduced by Volkersen [8] for load transfer in bonded joints and subsequently developed in the context of adhesive joint mechanics by Goland and Reissner [9]. Subsequent aerospace-focused analyses by Hart-Smith [10] further established the applicability of shear-lag models to thin adherends bonded by compliant layers. Modern expositions of this theory can be found in standard texts on adhesively bonded joints.

In the present formulation, the adhesive layer is modeled as a distributed shear foundation that transmits only shear stress between the foil and rigid substrate. The effective shear stiffness per unit area of the adhesive layer is expressed as:

$$k_s = G_{eff}/t_a \tag{12}$$

where t_a is the adhesive thickness, and G_{eff} is the effective shear modulus that accounts for possible through-thickness variations in adhesive properties.

When the shear modulus varies across the adhesive thickness, the effective modulus is defined by the harmonic mean of the local shear compliance as follows:

$$\frac{1}{G_{eff}} = \int_0^{t_a} \frac{dz}{G(z)} \tag{13}$$

The axial equilibrium of the thin foil relates the gradient of the axial stress to the adhesive shear stress as follows:

$$\frac{d\sigma(x)}{dx} = \frac{\tau(x)}{t_f} \tag{14}$$

where t_f is the foil thickness.

The thermally induced axial stress in the foil was introduced using the following eigenstrain formulation:

$$\sigma(x) = E_f \cdot \left(u'(x) - \alpha_f \Delta T_f\right) \tag{15}$$

where E_f and α_f are the Young's modulus and coefficient of thermal expansion of the foil, respectively; u is the displacement; and ΔT_f is the temperature increase in the foil.

The shear-lag parameter β is defined as:

$$\beta^2 = G_{eff}/\left(E_f \cdot t_f \cdot t_a\right) \tag{16}$$

The inverse of β represents the characteristic stress transfer length that controls the degree of thermal constraint imposed by the adhesive layer.

For a uniformly heated foil of length L with traction-free ends, the closed-form solution of the governing equation yields a hyperbolic axial stress distribution. The maximum compressive axial stress occurs at the mid-length of the foil and is given by:

$$\sigma_{max} = E_f \, \alpha_f \Delta T_f \, [1 - sech(\beta \, L/2)] \tag{17}$$

The corresponding adhesive shear stress distribution reaches its maximum magnitude at the foil ends. The maximum adhesive shear stress is expressed as:

$$\tau_{max} = E_f \, \alpha_f \Delta T_f \, t_f \, \beta \, tanh(\beta \, L/2) \tag{18}$$

These closed-form expressions provide a transparent and computationally efficient basis for estimating both foil axial stress and adhesive shear stress under extreme thermal loading and are particularly well suited for adhesive selection and preliminary design of high-aspect-ratio laminated structures.

Figure 5 shows the maximum normal stress in the SS 17-7PH foil calculated using Equation (17). The length of the foil was 50 cm, and its thickness was 0.076 mm. The SS 17-7PH yield and maximum strength at 450 C are shown for reference.

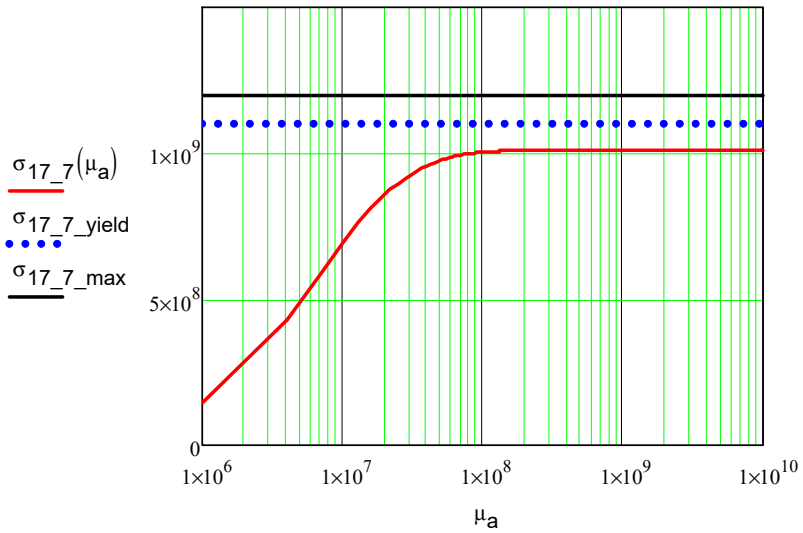


Figure 5. Dependence of the maximum stress in the ICD foil made of SS 17-7PH, σ_{17_7}, Pa, on, shear modulus of adhesive, μ_a, Pa.

The plateau in Figure 5 corresponds to the maximum thermal stress in the material. Flexible silicone-based adhesives have shear moduli below 10 MPa, and they can significantly reduce the maximum thermal stress in the metal foils of ICD. Ceramic- and silicate-based adhesives have shear moduli well over 100 MPa.

Figure 6 shows the maximum shear stress in the SS 17-7PH foil calculated using Equation (18). The foil length was 50 cm, and the thickness was 0.076 mm. Equation (18) was used.

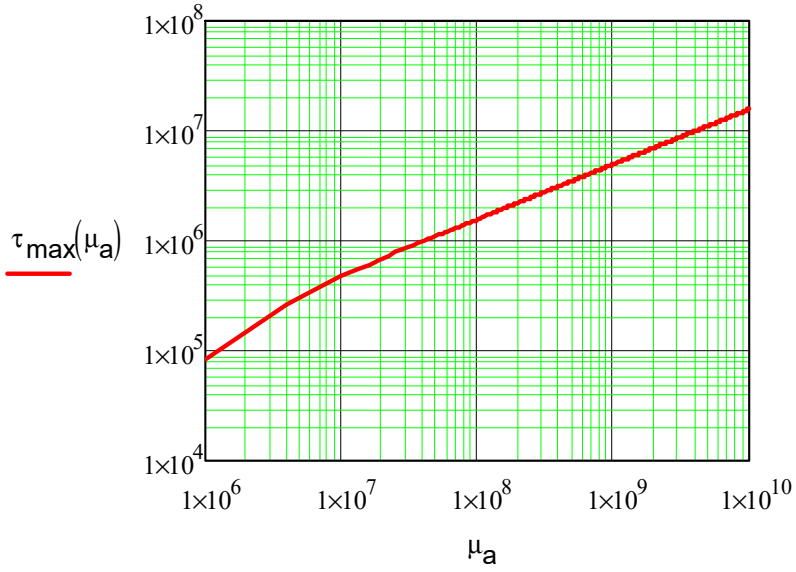


Figure 6. Dependence of the maximum shear stress in the ICD foil, SS 17-7PH (Pa), on the shear modulus of the adhesive, μ_a (Pa).

The maximum shear stress in the adhesive layer was equal to the maximum stress in the foil. The maximum thermal stress in the adhesive layer is $\sigma_{Ta} = \alpha_a \cdot \Delta T_f \cdot E_a$. The maximum total 2D stress in an adhesive layer is approximately equal to:

$$\sigma_{a_max} \approx \left(3\tau_{max}{}^2 + \sigma_{Ta}{}^2\right)^{\frac{1}{2}} \quad (19)$$

Figure 7 shows the dependence of the maximum and yield stresses in the ICD made of Ti grade 5 and Ti grade 4 foils. The solid red line represents the Ti grade 4 0.01 mm foil on 1 mm Cotronics 1531 silicone adhesive. The blue dotted line represents the Ti grade 5 0.01 mm foil on 1 mm silicate-based Cotronics 905 adhesive. The black-dashed line shows the yield strength of titanium grade 5 at 400 °C. The dash-dot crimson line shows the yield strength of titanium grade 4 at 400 °C.

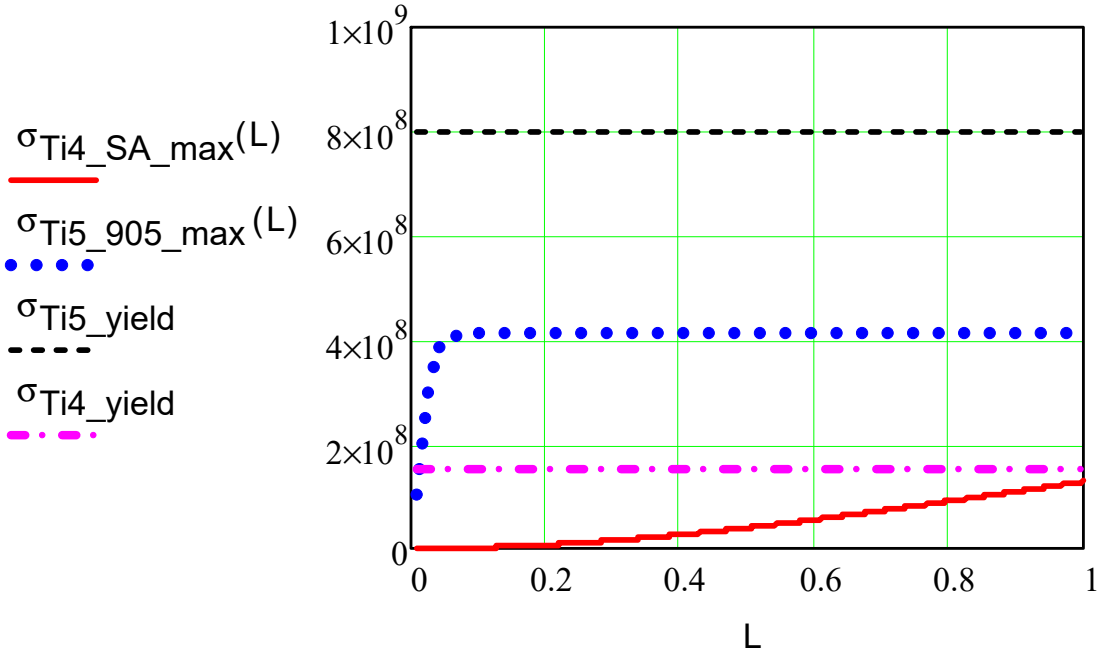


Figure 7. Dependence of the maximum and yield stress in the ICD made of Ti grade 5 and titanium grade 4 foils, σ_{max} (Pa), on foil length, m, at T_{max} = 400 °C.

The results of the foil stress calculations presented in Figure 7 confirm that grade 4 and grade 5 titanium foils on silicone adhesive can be safely used up to a 1 m-long strip, and that grade 5 titanium foil can also be safely used on silicate-based low-thermal-expansion Cotronics 905 adhesive (or Cotronics 940LE). The maximum and shear stresses using Equations (17)–(19) have been conducted for foils made of molybdenum, Invar, Inconel 783, SS 17-7PH, tungsten, two high-temperature silicone adhesives, and several silicate and ceramic adhesives. The metal foils were attached to a solid base using silicone or silicate-based adhesives. The selective results of the calculations and experimental results are presented in Section 3.

To avoid the thermal stress caused by the mismatch of the CTE in several laboratory ICDs, no adhesion was used, and the metal foils were pressed to the substrate either by magnetic pressure for ferromagnetic materials or by stretching the foil over a cylindrical cylinder, as described in Section 3.4. The adjacent moving layers of the ICDs glide over each other with friction. The friction force was calculated by multiplying the friction coefficient by the normal pressure. The maximum cavitation pressure should be added to thermal stress.

2.5. Cavitation Pressure of Water and Its Work on Ice Sheet

The experimental data on the cavitation pressure of water in the temperature range of 300–370 °C can be approximated using the following fitting formula:

$$P_{cav}(T_{ICD}) = \frac{221.2\ \text{bar}\cdot(T_{ICD} - 300\ ^\circ\text{C})}{70\ \text{K}} \tag{20}$$

where P_{cav} in Equation (12) is the fitting function of the experimental data [5,7]. Although the available cavitation threshold temperature data are scattered, their average is approximately (300 ± 10) °C. Hence, 300 °C was used in Equation (20).

The cavitation and saturation pressures of water vapor can reach 20 MPa at 370 °C. In ICDs this pressure was developed in a thin interfacial layer of melted ice. The formation of this high-pressure vapor layer (or bubbles) can induce further evaporation of the melted layer, and the resulting pressure expels the ice sheet from the ICD. The maximum work conducted on ice by the expanding cavitated layer was approximated under the assumption of purely adiabatic vapor layer expansion, which ceased when the vapor pressure decreased to atmospheric pressure. Equations (21)–(25) present the results of the maximum work calculations:

$$t_{cav}(T_{ICD}, \tau_p) = \ln\left(\frac{T_{ICD}}{300\ ^\circ\text{C}}\right)\cdot\lambda_w(\tau_p) \tag{21}$$

where t_{cav} is the thickness of the interfacial water layer heated over 300 °C:

$$V_0(T_{ICD}, \tau_p) = t_{cav}(T_{ICD}, \tau_p) \text{ is the initial vapor layer thickness :} \tag{22}$$

$$V_2(T_{ICD}, \tau_p) = t_{cav}(T_{ICD}, \tau_p)\frac{\rho_{cav}}{\rho_v} \text{ is the expanded vapor-layer thickness.} \tag{23}$$

Note that this layer is very thin: $V_2(330\ \text{K}, 0.1\ \text{ms}) = 0.33$ mm, $V_2(330\ \text{K}, 1\ \text{ms}) = 1.04$ mm:

$$W_{ad}(T_{ICD}, \tau_p) = \frac{P_{cav}(T_{ICD})\cdot V_0(T_{ICD}, \tau_p)^{\gamma}}{\gamma - 1}\cdot\left(V_0(T_{ICD}, \tau_p)^{1-\gamma} - V_2(T_{ICD}, \tau_p)^{1-\gamma}\right) \tag{24}$$

is the adiabatic work done by the water vapor:

$$v_{ice}(T_{ICD}, \tau_p, t_{ice}) = \frac{2W_{ad}(T_{ICD}, \tau_p)^{1/2}}{\rho_i t_{ice}} \tag{25}$$

is the expected maximum velocity of the ice layer. This assumes that all the work is performed on ice.

The experimental results presented in Section 3 better matched the theoretical calculations when the cavitation pressure in Equation (24) was replaced with the saturated pressure of water vapor [11]. This pressure was used in the theory vs. experiments comparison in Section 3.

Figure 8 shows the dependence of the initial thickness of the cavitating layer on the maximum temperature of the foil. The thickness of the cavitating layer is proportional to the square root of ICD thermal pulse length τ_p, (Equation (1) in the nomenclature list of variables). Increasing τ_p by either increasing C_C or by increasing the resistance of ICD foil increases ice fragments' velocity. However, this also increases the energy density requirement.

Figure 9 shows the estimated maximum velocity of a 5 mm thick ice sheet versus the maximum temperature of the metal foil T_{ICD}.

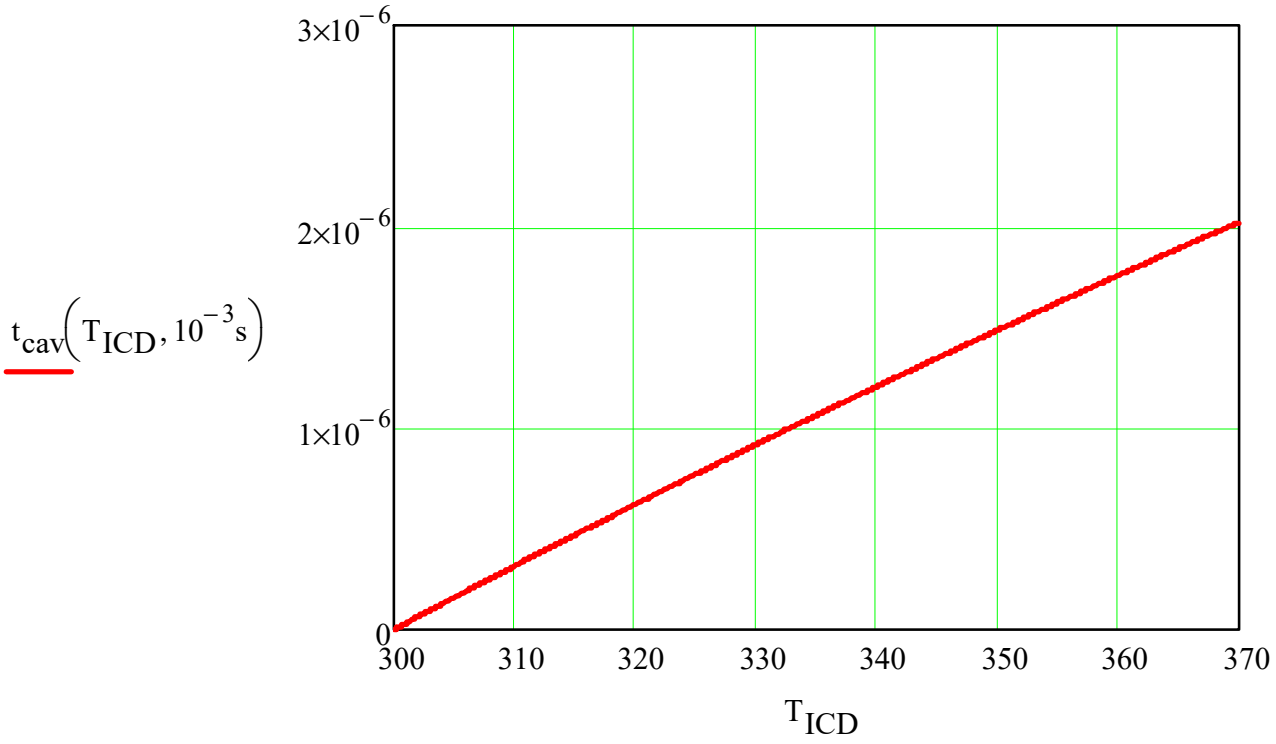


Figure 8. Thickness of cavitating layer, m, vs. cavitation temperature, °C. t_p = 1 ms. MathCad 15.

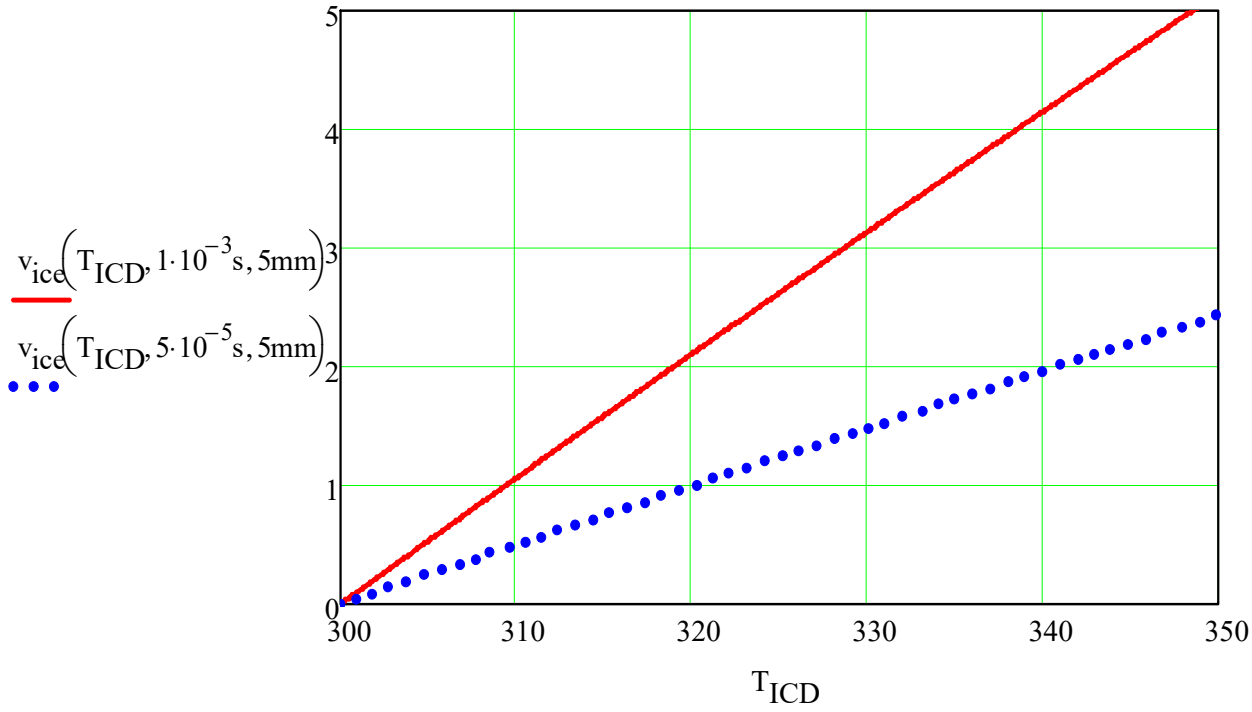


Figure 9. Ice velocity (m/s) versus cavitation temperature (°C). The thickness of the ice layer was 5 mm. t_p = 1 ms (red solid line), t_p = 0.05 ms (blue dotted line). MathCad 15.

2.6. Can ICD Break Ice Sheet?

An ICD must also break ice along its borders, as shown in Figure 10.

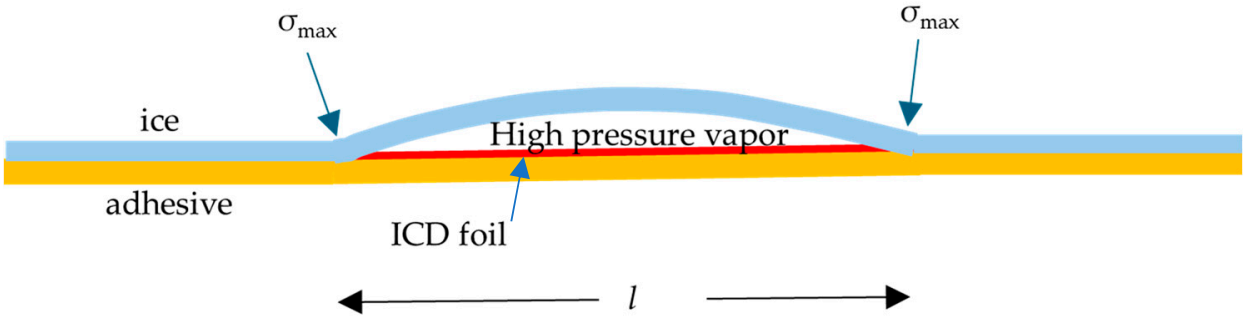


Figure 10. Breaking ice along ICD borders.

The maximum stress applied to ice at the ICD borders is approximately equal to:

$$\sigma_{max} \approx P_{cav} \cdot \frac{l}{2t_i} \tag{26}$$

To break the ice sheet, σ_{max} must exceed the bending strength of the ice. The latter is equal to 9 MPa for rime ice at −20 °C and 4.4 MPa for glaze ice at −5 °C [12]. For a typical value of l = 60 mm, ice thickness of 6 mm, and P_{cav} = 9.5 MPa (Equation (20), T_{ICD} = 330 °C) $\sigma_{max} \approx$ 47 MPa, thus breaking ice easily.

2.7. Effect of Convective Cooling and Aerodynamic Heating

Note that the density of the ICD heating power is approximately equal to:

$$P_{ICD} = \frac{Q_{ICD}}{t_p} \approx \frac{\frac{50\text{kJ}}{\text{m}^2}}{0.2\text{ ms}} = 250\frac{\text{MW}}{\text{m}^2} \tag{27}$$

Thus, P_{ICD} exceeds the air convective cooling power density [13,14] by four orders of magnitude. Therefore, the ICD heating of a foil by ΔT depends neither on airplane velocity nor on airfoil shape and thickness (Raynolds number). However, T_0 depends on the aerodynamic heating and air temperature.

In full-scale applications, the initial foil temperature T_0 of the ICD can differ from the air temperature because of aerodynamic heating. For instance, for a large airplane such as the Boeing 787, the temperature increase at a velocity of 800 km/hour can be approximately 30 °C, as calculated using NASA recommendations [15]. In large-scale applications, T_0 can be monitored by measuring the AC resistance of the foil. This technique is highly accurate and commonly used [16]. Monitoring T_0 and adjusting V_0 enable the ICD to maintain a target T_{ICD} temperature, such as 330 °C. ($\Delta T \sim V_0^{1/2}$).

2.8. COMSOL Multiphysics Simulation

The time-dependent Solid Mechanics and Heat Transfer were simulated using COMSOL Multiphysics 5.4 with the following modules: Heat Transfer in Solids and Fluids with Joule Heating and Phase Transition options, Solid Mechanics with Thermal Stress, Electrical Circuits, Electric Currents and Magnetic Fields.

Table 2 lists the parameters of the ICD made of a 17-7PH foil attached to a solid substrate with a 1 mm thick silicone adhesive. The parameters were used to build an actual ICD prototype and calculate the electrical current and foil temperature of an actual ICD prototype presented in 9th line of Table 3.

Table 2. COMSOL 5.4 Parameters used to model ICD made of 17-7PH SS.

T0	−10 [°C]	263.15 K	Ice initial temperature
t_SA	1 [mm]	1 mm	Silicone adhesive thickness
t_SS	3 [mil]	7.62×10^{-5} m	Foil thickness
t_ice	100 [um]	1×10^{-4} m	Ice thickness
dT	5 [K]	5 K	Phase transition width
V0	720 [V]	720 V	Initial capacitor voltage
C	1.5 [mF]	0.0015 F	Capacitor capacitance
l	15 [cm]	0.15 m	SS foil length
w	2 [cm]	0.02 m	SS foil width
R0	ro_e·l/(w·t_SS)	0.128 Ω	Foil resistance
Rc	0.0011 [ohm]	0.0011 Ω	Capacitor ESR
Rsw	0.0009 [ohm]	9×10^{-4} Ω	SCR (switch) ESR
Rw	(0.0077 + 0.003) [ohm]	0.0107 Ω	Lids and bus bars resistance
Lc	8.4×10^{-7} [H]	8.4×10^{-7} H	Total circuit inductance
Xi1	Rtot1·sqrt(C/Lc)/2	3	damping factor
Q	C·V0^2/(2·l·w)	130 kJ/m^2	ICD energy density, J/m^2
Rtot	ro_e·l/(w·t_SS) + Rc + Rw + Rsw	0.142 Ω	Total circuit resistance
Qevap	Q·R0/Rtot	108 kJ/m^2	ICD foil energy requirement

Table 3. Experimental and theoretical results. Not all test results are shown (over 100).

Foil	**Substrate**	**Size, mm**	**V_0, V**	**C_C, mF**	**Q_{exp}/Q_{theory} kJ/m^2**	**v_{exp}/v_{theory} m/s**
Invar	* Mica	0.03 × 31.2 × 107	550	1.5	68/68	≈1/5
Ti Grade 4	** Porcelain	0.05 × 20 × 158	570	1.5	77/77	≥6/5.2
Ti Grade 3	** Porcelain	0.01 × 37 × 75	790	0.1	11.25/11.25	≥2/1.4
SS 17-7PH	*** Mica	0.0762 × 20 × 140	760	1.5	155/155	≥8/8
SS 17-7PH	****	0.0762 × 15 × 150	600	1.5	120/120	≥6/7
SS 17-7PH	CA	0.0762 × 20 × 140	700	1.5	130/130	6.6/6.8
SS 17-7PH	** Porcelain	0.0762 × 20 × 150	750	1.5	140/140	≥10/10
SS 17-7PH	SA	0.0762 × 20 × 150	720	1.5	130/130	≥4/6
SS 430	*** Mica	0.054 × 18 × 91	460	1.5	97/97	≈2/1.8
SS 304	3M HT tape	0.0127 × 25.4 × 38	314	0.383	19.6/19.6	≈1/2.8
Cu/Kapton	** Porcelain	0.009 × 14 × 214	400	0.735	25.5/25.5	>2/5
Niobium	CA	0.03 × 12 × 118	320	1.5	54/54	≥1/5.8

* 0.1 mm mica film on a magnet paper sheet. B_r < 0.1T. ** Metal foil stretched over a Porcelain cylinder (D = 10 cm). This provided tight adhesive-less contact. *** 0.1 mm Mica film on a conformable magnet sheet for irregular surfaces, B_r = 0.42T. **** 0.1 mm Mica film on an array of small 2 mm × 5 mm × 20 mm Neodymium magnets N52, B_r = 1.2T. B_r is the magnetization provided by the supplier. CA is a mica-based ceramic adhesive #907 from Cotronics Inc. SA is a Permatex Optimum Red 399C silicone adhesive.

Figure 11 shows the time dependence of the current, and Figure 12 shows the time dependence of the maximum SS foil temperature. Figure 12 indicates that the interfacial

temperature reached 330 °C at 400 µs after most of the initial electric charge (approximately 90%) passed through the foil, as shown in Figure 10.

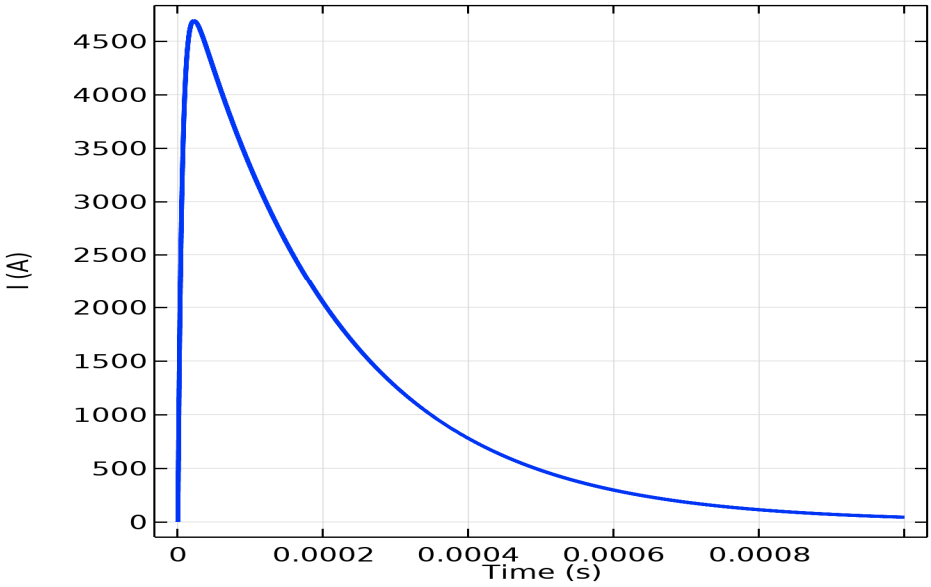


Figure 11. Electrical current, A, vs. time, s, COMSOL 5.4 simulation of 17-7PH stainless-steel ICD on mica laminate.

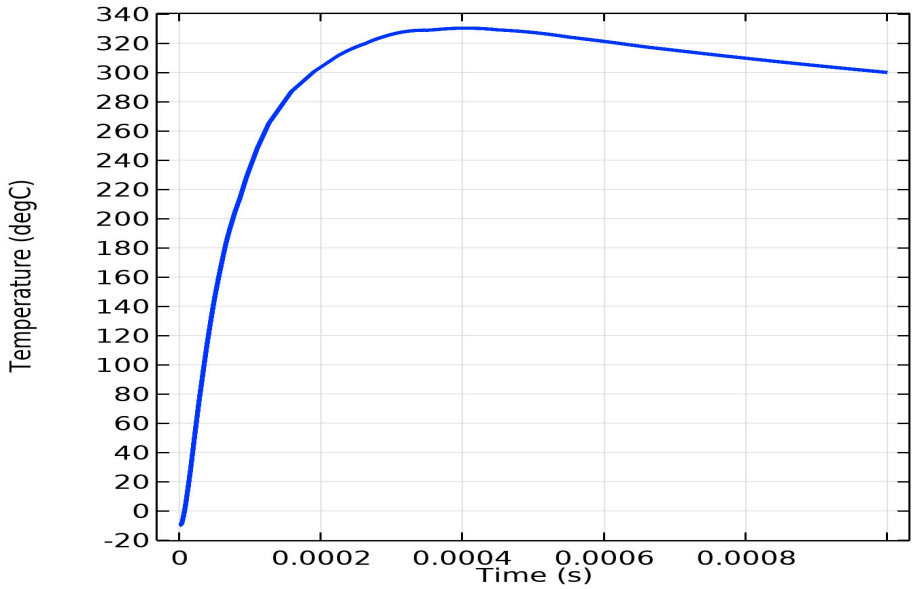


Figure 12. Maximum temperature of 17-7PHSS foil, degree C, vs. time, s, COMSOL 5.4 simulation of 17-7PH stainless steel/Permatex Optimum Silicone adhesive laminate ICD. $T_0 = -10$ °C.

Table 3 in Section 3 presents the calculation and experimental results for the selected ICDs. In all these examples, the initial foil temperature was $T_0 = -10$ °C, and the ICD maximum temperature was $T_{ICD} = 330$ °C. Silicone adhesives were either Permatex Optimum silicone adhesive substrate with $T_{max} = 399$ °C, or Cotronics Duraseal 1531 with $T_{max} = 427$ °C.

2.9. Summary of Materials Analysis

- Invar, tungsten, titanium grade 5, and SS 17-7PH have shear strengths higher than their maximum thermal stress at 400 °C. The foils made of these metals can be used with any HT adhesive analyzed in this study.

- Any metal foil analyzed in this study can be safely attached to a solid base using the two HT silicone adhesives analyzed.
- The main cause of thermal stress in the adhesive is the temperature gradient at the interface with the hot metal foil. Only two HT silicone adhesives, two Cotronics low-expansion silicate-based adhesives, and the composite-material silicate-based LOCTITE 2000 adhesive had strengths higher than their maximum thermal stress at 400 °C.
- Oxidation in air above 400 °C limits the use of tungsten, Invar, and titanium grade 5.
- The best among the metals were SS 17-7PH and Ti grade 4 on Cotronics 1531.
- The best among the adhesives were Cotronics 1531 silicone adhesive and Cotronics 905 and 940LE low-thermal-expansion silicate-based adhesives.

3. Experimental Work

All experiments were conducted at the Ice Research Lab of Petrenko-Multiphysics LLC. Various metals and metal alloys were investigated through theoretical calculations to identify the optimal foil and substrate materials for experimental testing. Eleven metals were selected for these experiments. The properties of all materials used in this study are listed in Appendix A Tables A1 and A2. The rationale for selecting the materials for laboratory testing is discussed below.

A detailed description of the experimental setup, materials, and electronics is provided in Sections 3.1–3.5. A general view of the ICD inside the refrigerator can be seen in the provided video clip. The author believes that this information is sufficient for followers of the method to set up their own experiments.

3.1. Metals Selection

Titanium Grade 4 (99% Ti) is the most used grade in the aerospace industry. It has a low $C_m \cdot \rho_m$ product, a CTE of approximately one half that of 304 and 316 SS, high corrosion resistance up to 426 °C, high strength of cold rolled temper, and high electrical resistivity.

Titanium Grade 3 was selected because of its low $C_m \cdot \rho_m$ product, low CTE, and high corrosion resistance. It is suitable for ICD testing when attached to a silicone adhesive.

The Invar (Ni 36%, Fe 64%) alloy was selected because of its exceptionally low CTE, high strength, mild corrosion resistance, ferromagnetic properties, and high electrical resistivity.

Stainless steels 304 and 316 are economical materials available in a wide range of thicknesses (starting from 0.005 mm and above). Under the "full-hard" condition, they offer high strength, corrosion resistance, and high electrical resistivity. However, their CTE values were higher than those of the SS 17-7PH and Inconel 783 alloys.

A 9 μm copper foil on 25 μm Kapton film laminate was chosen because of its very low energy requirement as an ICD device material. This commercially available DuPont product can endure short heating pulses of up to 400 °C.

17-7PH stainless steel was selected for its ferromagnetic properties, exceptional strength, high electrical resistivity, lower CTE than SS 304/316, and high corrosion resistance.

430 stainless steel was selected for its ferromagnetic properties, high strength, high electrical resistivity, and high corrosion resistance.

Nb was selected because it has the lowest $C_m \cdot \rho_m$ product and a low CTE, which matches that of the Resbond 907 ceramic adhesive used in this study. Nb exhibits high corrosion resistance and mechanical strength (cold-rolled foils).

Tungsten has a very low $C_m \cdot \rho_m$ product, a very low CTE, high mechanical strength, and good corrosion resistance.

Low-carbon 1008 steel has excellent magnetic properties and is easy and convenient to use in experiments. It is not corrosion-resistant and has a modest strength.

Inconel 783 has an exceptional combination of high strength, low CTE, and corrosion resistance.

3.2. Substrate Materials Selection

Adhesives that can withstand temperatures over 400 °C are primarily based on inorganic components, such as ceramics (CA), glass, or silicates (Si). These materials, while exceptionally heat-resistant (only when they were slowly heated), form rigid and brittle bonds with metals rather than elastic ones. They are also more likely to fail under thermal shock or stress because of their significant CTE and low flexibility. After evaluating many commercially available CA and SI adhesives, only three were chosen. The first was the LOCTITE MR 2000 composite adhesive manufactured by Henkel Co. According to the adhesive datasheet, its compressive modulus is 295 MPa or almost two orders of magnitude lower than that of ceramic adhesives. As shown in Table A2, the thermal stress in LOCTATE MR 2000 can be lower than its compressive strength. The second and third adhesives were Cotronics 905 and 940LE silicate-based very low CTE adhesives.

More opportunities arise from the use of two high-temperature silicone adhesives. The first is the Permatex Optimum silicone adhesive substrate with T_{max} = 399 °C, and the second is the Cotronics 1531 silicone adhesive with T_{max} = 427 °C.

3.3. Measurements of Ice Velocity

Two methods were used to measure the maximum initial velocity of the ice fragment. In the first method, video clips of ICD deicing were played frame by frame with 1/60 s between frames. During the ICD tests, the ice fragments were propelled rapidly away from the deicing surface. In many demonstrations, the fragments reached velocities on the order of 10 m/s. At typical smartphone frame rates (10–60 fps), the fragments move between 0.17 and 1 m per frame, leaving the field of view in 1–2 frames. This provides an insufficient temporal resolution for accurate frame-based tracking. Therefore, video footage was primarily used for the qualitative confirmation of ICD performance.

In the second method, the initial horizontal velocity v_{ice} was obtained using a simple ballistic equation. The ICD was positioned 1.0 m above the carpeted floor, and the horizontal travel distance x of the detached ice fragments was measured. Assuming a negligible initial vertical velocity, the flight time is determined by free fall:

$$t = \sqrt{\frac{2h}{g}} \tag{28}$$

where $h = 1.0$ m and $g = 9.81$ m/s^2.

The initial horizontal velocity is then expressed as

$$v_{\text{ice}} = \frac{x}{t} = x\sqrt{\frac{g}{2h}} \tag{29}$$

This method significantly improves the velocity precision compared to frame counting. For the demonstrated ICD configurations, the measured velocities were typically $v_{\text{ice}} \approx 1 - 10$ m/s, depending on the laminate design and the pulse parameters. These experimental results agree well with the theoretical estimates based on vapor expansion impulse generation.

3.4. Magnetic Support of Ferromagnetic ICD Foils

For quick and simple tests of the ferromagnetic foils, they were attached to solid substrates with magnetic shields, as shown in Figure 13. The maximum magnetization of

such shields was B_r = 1.45T for arrays of small N52 magnets. The magnetic pressure of a magnet array can apply to a thin ferromagnetic foil of thickness t_m can be approximated as

$$P_M = M_{sat} \cdot t_m \cdot \frac{B_r}{dz} \quad (30)$$

where dz is the approximate length of a magnetic field line from the N- to S-pole of a magnet.

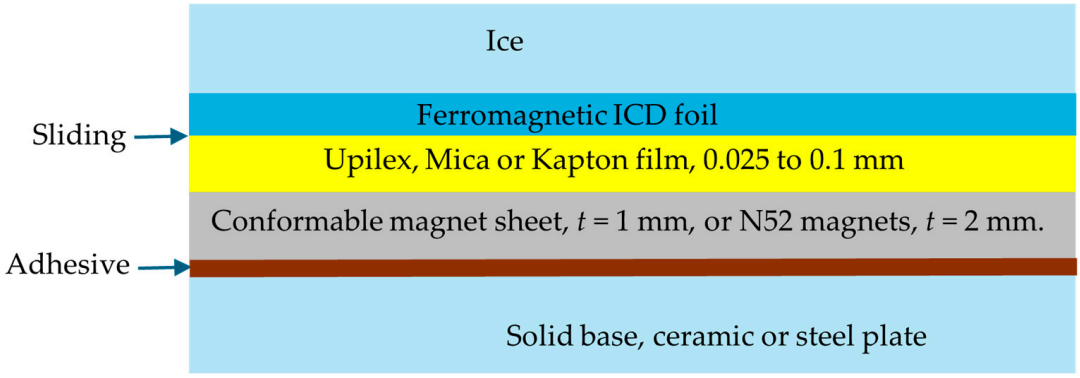


Figure 13. Magnetic attachment of ferromagnetic foils.

Using M_{sat} = 1.1 MA/m of 17-7PH stainless steel, foil thickness of t_m = 0.076 mm, B_r = 1.45T, and dz = 2.5 mm, P_M = 48 kPa is obtained. 2.5 mm for dz was chosen for an arrangement of 5 mm wide magnets with opposite directions of normal to the foil magnetization. COMSOL Magnetic Field modeling result was 50 kPa magnetic pressure for 0.05 mm Kapton film, which was in good agreement with the approximate Equation (30) result.

While keeping the foils in place, the magnetic support allowed the foils to expand and contract without significant thermal stress. The shear stress was limited by the friction coefficient of the material used. This attachment method worked very well in our laboratory tests, but it would require further theoretical and experimental validation before it can be recommended for actual aerospace applications. Some of the potential problems of magnetic support which future research should address are the wear of dielectric films by repetitive foil motion (≈1 mm amplitude), surface molecular instability of dielectric film materials, foil buckling, and the effect of normal and tangent air forces on foil position.

3.5. Electronics

Figure 14 shows the electric circuit used in this study. The MOC223 optocoupler isolates the low-voltage trigger circuit (left) from the high-voltage ICD circuit (right). The two diodes protect the capacitor and semiconductor-controlled rectifier (SCR) from reverse-voltage peaks. The peak capacitor discharge currents during testing varied from 200 A to 12 kA. The SCR consisted of four parallel BT158W thyristors, each capable of withstanding a 3 kA 1 ms current pulse with an I^2t rating of 6000 A^2s. Because of the low resistance of the tested ICDs, most connections were soldered, and 12 and 14 AWG leads were used to minimize the total resistance in high-current circuits. The capacitor charger module delivered an output power of 60 W with a maximum output voltage of 900 V. All the capacitors used in this study were film capacitors, featuring a very low estimated series resistance (ESR) of approximately 1 mΩ. The circuit shown in Figure 14 was used for several hundred pulses during the testing period. A two-channel digital oscilloscope recorded the voltage and current of the ICD, and a digital voltmeter monitored the capacitor voltage.

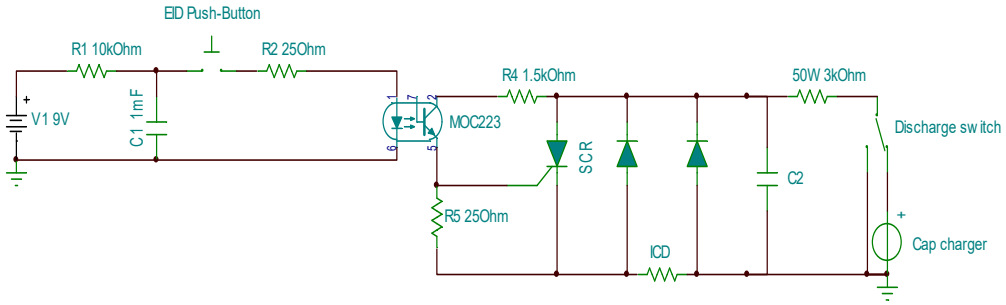


Figure 14. Schematic diagram of the electronics used to test the ICD prototypes.

3.6. Experimental Results

The results of the selected tests are presented in Table 3. The initial foil temperature for all tests was set to $T_0 = -10$ °C. The initial foil temperature was measured using a non-contact infrared laser thermometer.

In full-scale applications, the initial foil temperature T_0 of the ICD can differ from the air temperature owing to aerodynamic heating. For instance, for a large airplane such as the Boeing 787, the temperature increase can be approximately 30 °C, as calculated using NASA recommendations [15].

In large-scale applications, T_0 can be monitored using measurements of the AC resistance of the foil. This is a highly accurate and commonly used technique [17].

The successful performance of the ICDs was video recorded and is available in the Supplementary Media Files of this manuscript.

Table 3 presents the experimental and theoretical results for the seven types of tested ICD laminates. The ICD dimensions and aspect ratio of the foils were optimized using MathCad for the minimum energy requirement for the given foil and substrate materials, foil thickness, voltage $V_{0,}$ and capacitance C_C. The data enabled a comparison of the calculated and experimental total energy requirements and maximum ice-fragment velocities. The total energy requirement was identical because it was given by C_C and $V_{0,}$ and foil area. The details of the laminations are as follows: The calculated and experimental ice velocities were very close for ferromagnetic steels (SS 17-7PH and SS 430) and titanium ICDs. For the Cu/Kap laminate, ice pieces left the field of view (0.2 m) in less than 0.1 s, which corresponds to $v \approx 2$ m/s/s. For the SS 304- and Niobium-made ICD, the experimental v_{ice} velocities were significantly lower than the calculated velocities. The details of the substrates used are as follows:

The maximum normal pressure of the magnet was $B_r{}^2/(2\mu_0)$. However, owing to the small thickness of the ferromagnetic foil, the actual pressure was lower than the calculated value. The actual normal pressure was calculated using the COMSOL Multiphysics software and using Equation (30).

All ICDs, which were constructed from the selected materials and designed according to the theoretically calculated parameters, successfully demonstrated the ice cavitation phenomenon. The best deicing performance was observed with 0.0762 mm thick 17-7PH stainless steel and titanium Grade 4 0.05 mm thick foil, which exhibited the highest ice expulsion velocity of 6–10 m/s.

The lowest energy consumption for the ICDs was achieved using the thinnest foils. However, the thinnest SS foil lacked durability and exhibited signs of strain after several ICD pulses were applied. The Cu/Kapton laminate produced by DuPont did not exhibit signs of strain after 25 ICD-pulse tests, and neither did 10 μm Ti foil, which was stretched over a ceramic cylinder. The lower was the product of the material density and specific heat capacity, the lower was the energy requirement for the ICD.

The best ICD performance was achieved when a metal foil was attached to a rigid substrate, such as a cylindrical solid ceramic surface (** porcelain), Cotronics 907 ceramic adhesive (CA), and an array of small neodymium magnets (N52) (****).

Figure 15 shows the dependence of the ice fragment velocity on the estimated maximum temperature of the SS foil. The thermal time constant of the stainless-steel ICD was 0.15 ms. The data were collected from the test results of ICDs made of stainless steel 17-7PH. The maximum foil temperature was calculated using the ECL equation. The ice velocity increased with increasing maximum foil temperature and t_p, which agrees with the theory.

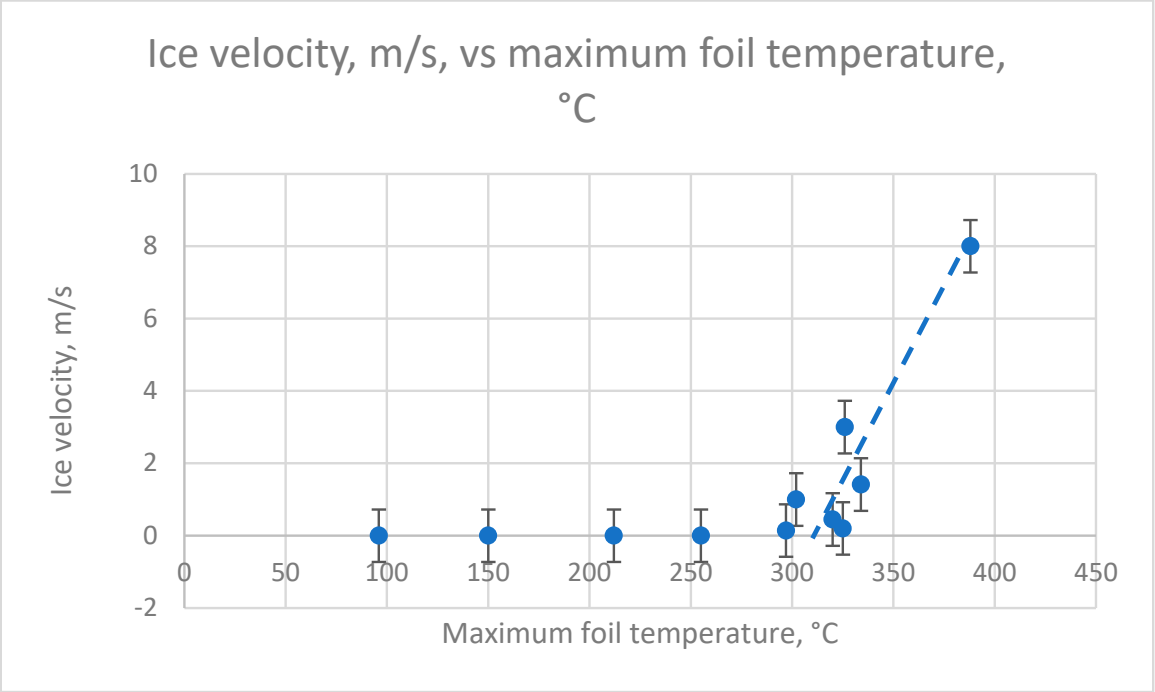


Figure 15. Approximate velocity of ice fragments, m/s, versus maximum SS foil temperature, °C.

Ice cavitation effectively separated the ice from all the metal foils. The theoretical predictions and experimental results showed reasonable agreement, suggesting that the developed theory could be beneficial for future practical applications of ice cavitation.

While the trend line in Figure 15 points at *a* T_{cav} of 310 ± 10 °C, it may be lower on highly hydrophobic surfaces. Thomas et al. [17] observed that T_{cav} depends on the hydrophobicity or hydrophilicity of the surface. For highly hydrophobic coatings (e.g., $CH_3(CH_2)_{15}SH$), cavitation occurred at temperatures as low as 187–197 °C. They also noted a reduction in T_{cav} with an increase in the heating pulse duration. This observation is not surprising, because prolonged heating eventually causes water to boil at 100 °C. Most experimental data on T_{cav} originate from studies using gold and platinum wires as heaters, with electric pulse lengths ranging from 1 to 5 µs. In contrast, our experiments used much longer heating pulses, ranging from 30 µs to 1 ms.

The reduction of T_{cav} (our T_{ICD}) can be used to further reduce the ICD energy requirement, as shown in Equation (3) and Figure 4.

The ice fragment velocities presented in Figure 15 agree with the theoretically calculated velocities presented in Figure 8 and with the experimental results presented in Table 3.

Niobium and titanium foils demonstrated a low ICD energy requirement and good de-icing performance, making them strong contenders for material selection. Moreover, the CTE of Nb closely matched that of the 907-ceramic adhesive.

The lowest experimentally observed ICD energy requirement, 11.25 kJ/m^2, was found for the very thin (0.01 mm) titanium ICD. However, titanium is the most challenging material to work with, because soldering titanium instantly creates a thick and poorly conductive oxide layer. Nickel bus bars were successfully attached to titanium foils using an ultrasonic solder and the solder alloy, Cerasolzer 217, which was developed specifically for soldering titanium. Unfortunately, the initially low resistance of the nickel busbars (1 mΩ) increased significantly after several ICD pulses, following the degradation of the ICD performance. Durable low-resistance electrical connections to titanium require titanium electroplating with Ni. However, only a limited number of companies worldwide claim to have the capability to electroplate titanium with nickel, and their services are prohibitively expensive for laboratory-scale testing. Nevertheless, the excellent performance of ICDs made of titanium Grades 3 and 4 ($v_{ice} \geq 6$ m/s) and the modest energy requirement ($\leq$77 kJ/m^2) make titanium attractive for this application.

Invar-made ICDs demonstrated reproducible results, although their performance was weak. For ICD applications, Invar offers high electrical resistivity (8.2×10^{-7} Ω·m), sufficient yield strength (260 MPa at 400 °C), modest corrosion resistance, and ferromagnetism. Invars can also be easily soldered. The magnetic properties of Invar foils allow them to be attached to substrates without adhesives, thereby avoiding high thermal stress. However, the ferromagnetism of Invar diminishes above a temperature of 279 °C. The very low temperature-average CTE of Invar (2.5×10^{-6} K^{-1}) results in a relatively low thermal stress, even when a ceramic adhesive is used. Owing to the high strength of Invar, thin Invar foils should also withstand rain-erosion tests. ICDs made of 0.008 mm (commercially available Invar foil thickness) have a very low energy requirement of 28 kJ/m^2, making Invar a strong candidate for ICD applications. These thin Invar foils must be bonded to a solid substrate using Cotronics 905 or Cotronics 940LE adhesives. Invar exhibits limited corrosion resistance at temperatures below 450 °C.

The ICD made of very thin 304 stainless steel demonstrated a very low energy requirement. However, 304 stainless steel has a relatively large CTE and insufficient strength (Table A1). This steel cannot be used in large-scale applications.

The ICD made of 430C stainless steel demonstrated an acceptable ICD performance. However, 430C stainless steel has insufficient strength (Table A1). This steel cannot be used in large-scale applications.

The best overall performance was observed for ICDs made of martensitic 17-7PH stainless steel. This steel has exceptional strength, a modest CTE, and high corrosion resistance. The ICD made of this steel can be attached to substrates using two silicone adhesives and two silicate-based low-thermal-expansion adhesives.

The copper/Kapton laminate (Pyralux AC by Dupont Co., Circleville, OH, USA) exhibited the third-lowest energy density requirement of 25.5 kJ/m^2. However, copper has a very low yield strength and cannot be used for large-scale applications.

3.7. Absence of Cavitation Damage (CD)

Numerous experiments with ICDs have been conducted since 2005, the year of the patent application, including testing over 50 combinations of metals and substrates at various temperatures, power rates, and energy densities. The overall number of tests was over 1000. However, no signs of cavitation damage were observed. (Hundreds of cavitation damage images are available on the web for comparison). A video clip of the ICDs in action is provided. The video shows the 35th test of a 17-7PH cold rolled 3 mil thick foil placed on Cotronics 907 CA. No CDs were observed. The maximum steam pressure of the thin water film cavitation (1–20 MPa) was much lower than the strength of ICD foils. Moreover, no published images of CD formed at temperatures of 300 °C or higher were found. The

commonly observed CDs occurred at temperatures below the water boiling point, when the negative cavitation pressure was very large (170 MPa to 200 MPa). This high pressure is one to two orders of magnitude higher than the maximum steam pressure created by the ICD pulse.

4. Feasibility of a Full-Scale ICD

The ICD dimensions used in our laboratory tests were selected to fit the dimensions of our refrigerators and the specifications of our high-voltage electronics. However, can ICDs deice a large aircraft? To answer this question, the following calculations were conducted using the dimensions of the ice-protected areas of the Boeing 787-9 aircraft [14].

A_{ice} = 20.95 m^2 is the total ice-protection area of the Boeing 787. The area was divided into eight slats for cyclic deicing.

$A_{ps} = A_{ice} \cdot 0.19$ = 3.98 m^2 is the total parting strip area that was continuously heated, and $t_{deicing}$ = 3 min is the recommended period for cyclic deicing [15].

For the ICD operations, three 3.0 mF × 1100 V thin-film capacitors (EPCOS-TDK) were selected. Each capacitor was assigned one-third of the A_{ps}. (assuming two wings and a stabilizer area). A 0.025 mm thick SS 17-7PH foil with Cotronics 905 silicate-based low-thermal-expansion adhesive was selected as the ICD material.

C_C = 3 mF.

V_C = 1100 V is the initial voltage of the capacitor.

3.0 mF capacitor powers the two connected ICD sections in parallel, 1.5 mF per section.

Q_{tot} = 50 kJ/m^2 is the total ICD energy density requirement.

$W_{ICD} = Q_{tot}/t_{deicing}$ = 278 W/m^2 is the time-averaged ICD power requirement.

Assuming a 90% efficiency of the capacitor chargers, the time-averaged ICD power requirement is:

$W_{ICD_total} = W_{ICD}/0.9$ = 309 W/m^2

This number (309 W/m^2) is 60 times lower than the 18.60 kW/m^2 recommended by the SAE for the continuous heating of the parting strips.

The energy stored in the capacitor was $QC = CC \cdot VC2/2$ = 1.815 kJ.

$A_{ICD} = Q_C/Q_{tot}$ = 0.036 m^2 is the area of ICD section.

$N_{ICD} = A_{ps}/A_{ICD}$ = 111 is the total number of ICD sections, that is, 37 sections per capacitor.

The total time required to deice the parting strips is limited by the charging time of one capacitor multiplied by the number of ICD sections per capacitor.

P_{charge} is the capacitor charger output power, and

$t_{charge} = Q_C/(P_{charge} \times 0.9)$ is the time required to charge the capacitor, assuming 90% efficiency.

$t_{ICD} = t_{charge} \cdot N_{ICD}/3$ is the total time required to deice all parting strips.

With 9 kW (3 kW per charger) delegated to the ICD system, the total time was 25 s, which is a small fraction of the de-icing cycle (180 s). For comparison, the Boeing 787 has two generators with a total power output of 500 kW. The A320 Airbus Airplane has an electric power of 180 kW. Increasing the total deicing time of the ICD to 3 min reduced the average total ICD power requirement to 1.2 kW.

Note that the 3 mF film capacitor has an Equivalent Serial Resistor) of 1 mohm, which is approximately 1% of the ICD ESR. Thus, only a few watts will be dissipated inside the capacitor. The capacitor has a weight of approximately 2 kg and does not overheat.

In the above estimates the ICD pulse length, which is less than 1 ms, was neglected.

The high voltage of 1100 V can be reduced by using aluminum electrolytic capacitors of similar size and weight as the 3.0 mF × 1100 V film capacitor. For instance, a 39 mF × 500VDC HCG FA capacitor manufactured by Hitachi can store 4875 J of electrical energy. This is almost three times more than the energy stored in a 3 mF × 1100 V capacitor.

The 18 mF × 400 V capacitor by Nippon Chemi-Con closely matched the energy stored in the 3.0 mF × 1100 V capacitor. As a reference, the onboard voltage of 240VAC is commonly used in aviation, and it has a 340 V amplitude.

The maximum ICD temperatures of 350–450 °C were well below the aircraft engine exhaust temperature of 788–955 °C.

Combining an ICD for parting strips with a synchronized PETD for the remaining iced areas of the airfoils can significantly reduce the energy and power consumption required for aircraft deicing.

The integration of the ICD into an entire aircraft deicing system is the focus of our ongoing research. However, owing to the very low power and energy requirements, the ICD can perform deicing of the total icing area instead of being complementary to the PETD or cyclic deicing. An important next stage of ICD R&D is testing it in an icing wind tunnel.

5. Conclusions

This study introduces and experimentally validates the Ice Cavitation Deicer (ICD), a new deicing technology capable of removing ice from the leading edge of airfoils with extremely low energy consumption. The ICD uses short, intense thermal pulses to superheat a thin interfacial melt layer and generate a cavitation impulse in the range of 1–10 MPa. The impulses were sufficient to fracture and eject the ice in the direction normal to the surface. Cavitation impulses accelerate ice fragments to 5–10 m/s, ensuring rapid detachment. Theoretical calculations accurately predicted foil heating, melt-layer thickness, cavitation pressure, thermal stress of ICD materials, and uplift velocity, validating the theoretical framework.

The ICD operation reduces the average deicing power by approximately two orders of magnitude compared to the continuous electrothermal heating of the stagnation line. The selected metal foils and adhesives withstood repeated thermal cycling, demonstrating their suitability for long-term aerospace operations.

Overall, the Ice Cavitation Deicer provides a compact, energy-efficient, and highly effective method for removing stagnation line ice. Its low power requirements, rapid response, and compatibility with thin-foil heater architectures make it a promising technology for both conventional and electrified aircraft, UAVs, rotorcraft, and other platforms where power availability is limited. Future work will focus on scaling the ICD to full leading-edge geometries, optimizing the laminate structures, integrating the system into flight-capable prototypes and testing it in an icing wind tunnel.

Supplementary Materials: The following supporting information can be downloaded at: https://www.mdpi.com/article/10.3390/aerospace13030217/s1, Video S1. Stainless-steel foil on a ceramic adhesive. A stainless steel 17-7PH foil was attached to a ceramic plate using ceramic adhesive (907 by Cotronics Inc.). The foil dimensions were 0.076 mm × 20 mm × 150 mm. C_C = 1.5 mF, V_0 = 760 V, Q_{tot} = 144 kJ/m^2, T_{air} = −10 °C. Ice cubes measuring 10 mm × 10 mm × 10 mm were attached to the foil with rapidly freezing water drops. The initial velocity of the ice fragments exceeded 10 m/s.

Funding: This research was funded by Petrenko-Multiphysics, LLC.

Data Availability Statement: Data supporting the findings of this study are available from the author upon reasonable request.

Acknowledgments: The author gratefully acknowledges the funding and laboratory facilities provided for this research by Petrenko-Multiphysics LLC.

Conflicts of Interest: The author declares no conflicts of interest. The author is an inventor of patents related to the deicing technologies described in this study.

Appendix A

Table A1. Properties of metals at 400–450 °C.

Material	ρ	C	α	ρ_e	k	E	$\sigma_{yield\ at}$ 400 °C	$\sigma_{ts\ at}$ 400 °C
Units	kg/m^3	J/kg·K	K^{-5}	10^{-8} Ω·m	W/m·K	GPa	MPa	MPa
Invar, as rolled, $T_{max} \leq 400$ °C	8100	515	0.3	82	10.2	125	240–280	140
SS 17-7PH, CH900 $T_{max} = 482$ °C	7800	460	1.1	83	16.4	204	1200	780
Ti Grade 5, TH1050 $T_{max} \leq 400$ °C	4430	526	0.85	178	7	114	800	400
Ti Grade 4 as rolled $T_{max} = 426$ °C	4540	523	0.85	56	17	116	150	360
Tungsten cold rolled $T_{max} \leq 400$ °C	19300	134	0.4	5.4	163	300	600–700	625
Molybdenum TZM $T_{max} = 400$ °C	10220	217	0.5	5.3	130	330	650–780	700
Inconel 783 $T_{max} = 700$ °C	7810	435	11	120	11.4	173	750	727
SS 304 full hard	7900	450	1.7	72	17.3	200	140	1384
SS 430C	7740	460	1.1	60	26	200	190	864
Nb cold rolled $T_{max} \leq 400$ °C	8570	268	0.7	16	53	103	300	288

The mechanical properties of metal and metal alloy foils are strongly dependent on the details of their manufacturing, such as being as-rolled, annealed, or cold rolled.

SS 17-7PH CH900 temper is a cold-rolled material heat-treated at 900 °F (482 °C) for one hour after forming.

Table A2. Properties of substrate materials.

Substrates	ρ	C	α	T_{max}	k	E	$\sigma_{yield\ at}$ 400 °C	$\sigma_{ts\ at}$ 400 °C
Units	kg/m^3	J/kg·K	K^{-5}	°C	W/m·K	GPa	MPa	Mpa
SA, Cotronics	998	1465	2	427	0.3	0.0012	1.9	0.01
SA, Permatex	1180	1050	30	399	0.2	0.0014	≈5.5	0.14
Kapton	1420	1090	1.7	400	0.12	2.5	234	17
Cotronics 905	1310	800	0.054	1370	1.44	≈7.5	22	0.0016
Cotronics 940LE	1310	800	0.072	1370	0.72	≈7.5	24	0.0021
Zr ceramic flex ribbon	6000	540	1.08	1000	2.7	210	1000	860
Upilex	1400	1100	2.0	≤450	0.13	7.5	530	52
Loctite 2000	1540	NA	0.7	1000	1.2	0.3	2.4	0.83
Anodized Ti	≤4000	683	≈0.85	≥700	≈2.3	≈40	≈3500	140

References

1. Petrenko, V.F. Systems and Methods for Modifying an Ice-To-Object Interface. U.S. Patent 6870139, 2005.
2. Petrenko, V.F.; Sullivan, C.R.; Kozlyuk, V.; Petrenko, F.V.; Veerasamy, V. Pulse electro-thermal de-icer (PETD). *Cold Reg. Sci. Technol.* **2011**, *65*, 70–78. [CrossRef]
3. Khodakarami, S.; Agarwal, V.; Kabirzadeh, P.; Solecki, A.; Hoque, M.J.; Yang, W.; Stokowski, N.; Jacobs, J.; Chatterji, A.; Lovelace, E.; et al. Aircraft Electrothermal Pulse Deicing. *J. Heat Mass Transf.* **2025**, *147*, 012401. [CrossRef]
4. Caupin, F.; Herbert, E. Cavitation in water: A review. *Comptes Rendus Phys.* **2006**, *7*, 1000–1017. [CrossRef]
5. Caupin, F. Liquid-vapor interface, cavitation, and the phase diagram of water. *Phys. Rev.* **2005**, *71*, 051605-1–051605-5. [CrossRef] [PubMed]
6. Petrenko, V.F. Pulse Systems and Methods for Detaching Ice. U.S. Patent 7703300, 27 April 2010.
7. Magaletti, F.; Gallo, M.; Casciola, C.M. Water cavitation from ambient to high temperatures. *Nat. Portf. Sci. Rep.* **2021**, *11*, 1–10. [CrossRef] [PubMed]
8. Volkersen, O. Die Nietkraftverteilung in zugbeanspruchten Nietverbindungen mit konstanten Laschenquerschnitten. *Luftfahrtfor Schung* **1938**, *15*, 41–47.
9. Goland, M.; Reissner, E. The stresses in cemented joints. *J. Appl. Mech.* **1944**, *11*, A17–A27. [CrossRef]
10. Hart-Smith, L.J. *Adhesive-Bonded Single-Lap Joints*; NASA CR-112236; NASA: Washington, DC, USA, 1973.
11. Incropera, F.P.; DeWitt, D.P. *Heat and Mass Transfer*, 5th ed.; John Wiley & Sons: Hoboken, NJ, USA, 2002; pp. 924–925.
12. Fallon, C.; Truyen, E.; Eakins, D.; Pervier, H.; Pervier, M.L.; Lopez, M.A. The effect of accretion temperature on microstructure and bending strength of atmospheric ice. *Mater. Today Commun.* **2023**, *37*, 107461. [CrossRef]
13. Meier, O.; Scholz, D. *Handbook Method for Estimating Power Requirements for Electrical De-Icing Systems*; Hamburg University of Applied Sciences: Hamburg, Germany, 2010; Available online: https://www.fzt.haw-hamburg.de/pers/Scholz/MOZART/MOZART_PUB_DLRK_10-08-31.pdf (accessed on 3 September 2025).
14. SAE. *Ice, Rain, Fog, and Frost Protection*; Society of Automotive Engineers: Warrendale, PA, USA, 1990.
15. Isentropic Flow. Available online: https://www.grc.nasa.gov/www/k-12/airplane/isentrop.html (accessed on 3 September 2025).
16. Bentley, J.P. *Principles of Measurement Systems*, 4th ed.; Pearson Education: Harlow, UK, 2005; Chapter 8.
17. Thomas, O.C.; Cavicchi, R.E.; Tarlov, M.J. Effect of Surface Wettability on Fast Transient Microboiling Behavior. *Langmuir* **2003**, *19*, 6168–6177. [CrossRef]

Disclaimer/Publisher's Note: The statements, opinions and data contained in all publications are solely those of the individual author(s) and contributor(s) and not of MDPI and/or the editor(s). MDPI and/or the editor(s) disclaim responsibility for any injury to people or property resulting from any ideas, methods, instructions or products referred to in the content.